Segment piston estimation using sequential phase retrieval

Marcos A. van Dam[a], Jesse Cranney[b], and Antonin H. Bouchez[c]

[a]Flat Wavefronts, 21 Lascelles Street, Christchurch 8022, New Zealand
[b]Advanced Instrumentation and Technology Centre,
Research School of Astronomy and Astrophysics, the Australian National University,
Mount Stromlo Observatory, Weston ACT 2611, Australia
[c]GMTO Corporation, 300 N. Lake Avenue, Pasadena, CA 91101, USA

ABSTRACT

The Giant Magellan Telescope (GMT) consists of seven 8.4-m diameter circular segments in a close-packed pattern to create a telescope with an effective diameter of 25.4 m. The Laser Tomography Adaptive Optics system for the GMT uses six Shack-Hartmann wavefront sensors observing six laser guide stars (LGSs) to measure high-order wavefront aberrations. LGS-based adaptive optics systems also require one or more tip-tilt sensors, since the LGSs are affected by tip-tilt errors on the uplink. The wavefront errors also contain segment piston, which can be induced by the atmosphere or the telescope but cannot be sensed by the Shack-Hartmann wavefront sensors. If the tip-tilt sensor is a Nyquist sampled imager, we can use phase retrieval to measure segment piston at the full frame rate of the tip-tilt sensor. Two existing algorithms, Gerchberg-Saxton and the Fast & Furious algorithms, are adapted for this purpose. We demonstrate using end-to-end simulations that phase retrieval can be used to measure segment piston and thus improve the delivered image quality over a range of operating conditions.

Keywords: Giant Magellan Telescope, segment phasing, adaptive optics, laser tomography adaptive optics, phase retrieval, Gerchberg-Saxton, Fast & Furious

1. INTRODUCTION

The Giant Magellan Telescope (GMT) consists of seven 8.365 m circular segments with a separation of 8.710 m between the central segment and the outer segments (Fig. 1). The GMT is a Gregorian design with an adaptive

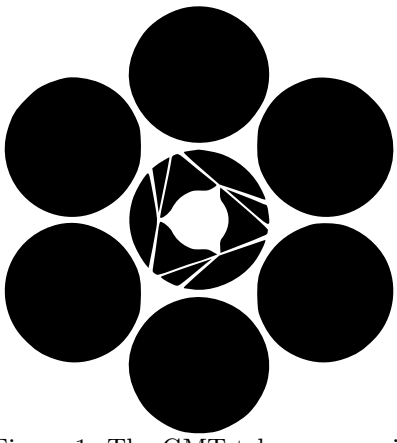

Figure 1: The GMT telescope pupil

secondary mirror (ASM). The ASM is also segmented, with the segments critically sized with respect to the primary mirror segments. The design of the GMT is ideal for ground-layer adaptive optics, high contrast imaging and imaging at thermal infrared wavelengths.

Send correspondence to Marcos van Dam, e-mail: marcos@flatwavefronts.com

In order to form images at the diffraction limit of the telescope (equivalent to a diameter of approximately 25.4 m), it is crucial to phase the total optical path of each primary-secondary mirror pair to a small fraction of the imaging wavelength. The GMT has two diffraction-limited adaptive optics (AO) modes which require a phased telescope.[1] The natural guide star adaptive optics (NGAO) mode guiding on a visible light pyramid wavefront sensor is used when there is a sufficiently bright star within approximately 30″ from the science target. For greater sky coverage, there is also a laser tomography adaptive optics (LTAO) system that employs six side-projected laser guide stars (LGSs), along with a single natural guide star (NGS) used to measure tip-tilt. This tip-tilt star can be much fainter and further away from the science target than the guide star used in NGAO mode. In addition, it is envisioned that most other observations will benefit from correction using the ground-layer adaptive optics (GLAO) mode. Phasing the telescope in GLAO mode does not significantly improve the delivered image quality.

Two first generation instruments are fed LTAO-corrected wavefronts: the Giant Magellan Telescope Integral Field Spectrograph (GMTIFS)[2] and the Giant Magellan Telescope Near Infrared Spectrograph (GMTNIRS).[3] Each instrument is equipped with its own on-instrument wavefront sensor (OIWFS) that guides on an NGS. The OIWFS is required to make tip-tilt measurements at 500 Hz, focus measurements at 10 Hz and high-order truth measurements at 0.03 Hz in order to recover the modes that the laser tomography wavefront sensor (LTWS) is not able to measure. The tip-tilt sensor in the OIWFS consists of a Nyquist sampled imager operating at K-band (2.179 µm. The GMTNIRS OIWFS uses about 10% of the light from the on-axis science target, with the remainder of the light sent to the spectrograph. GMTIFS uses a pick-off mirror to send all of the light from a guide star situated between 15″ and 90″ off-axis to the OIWFS. A dedicated deformable mirror (DM) is used to correct the high-order anisoplanatism in the direction of the tip-tilt star.

This paper investigates the feasibility of using the tip-tilt sensing images as a segment piston sensor. The motivation for this paper is most easily understood via inspection of Figure 2. Uncorrected phasing errors in the primary mirror segments of the GMT degrade the point spread function (PSF) of the science images. Figure 2 displays some simulated residual wavefronts, with and without the use of segment piston correction based on the tip-tilt sensor images, along with the corresponding PSFs.

This paper extends recent work by Cranney *et al.*, where a novel method based on Moving Horizon Estimation (MHE) was developed and compared to the Fast & Furious (F&F) algorithm.[4] The increased complexity of MHE, unfortunately does not lead to improved segment piston control. In this paper, we compare F&F to a sequential phase retrieval algorithm based on the well-known Gerchberg-Saxton algorithm.[5,6]

The remainder of the paper is distributed as follows. Section 2 describes the entire segment phasing strategy of the GMT in LTAO mode to add context to this work. The phase retrieval algorithms are described in Section 3. The simulations are described in Section 4, with the results presented in Section 5. Finally, conclusions are drawn in Section 6.

2. SEGMENT PHASING STRATEGY IN LTAO MODE

The wavefront control for the GMT is described in detail in Bouchez *et al*,[7] while Quirós-Pacheco *et al* focus on segment piston control for the NGAO mode.[8] The NGAO mode has a pyramid wavefront sensor (WFS), which is sensitive to segment piston when the wavefront correction is good. However, the LTAO mode uses Shack-Hartmann WFSs which are not sensitive to segment piston errors. In this section, we describe the phasing strategy for the GMT operating in LTAO mode.

It is instructive to first consider the source of the segment piston errors:

(i) M1 and M2 position errors,

(ii) windshake and vibrations of M1 and M2 segments, and

(iii) atmospheric segment piston,

as well as the three sensors used to measure these errors:

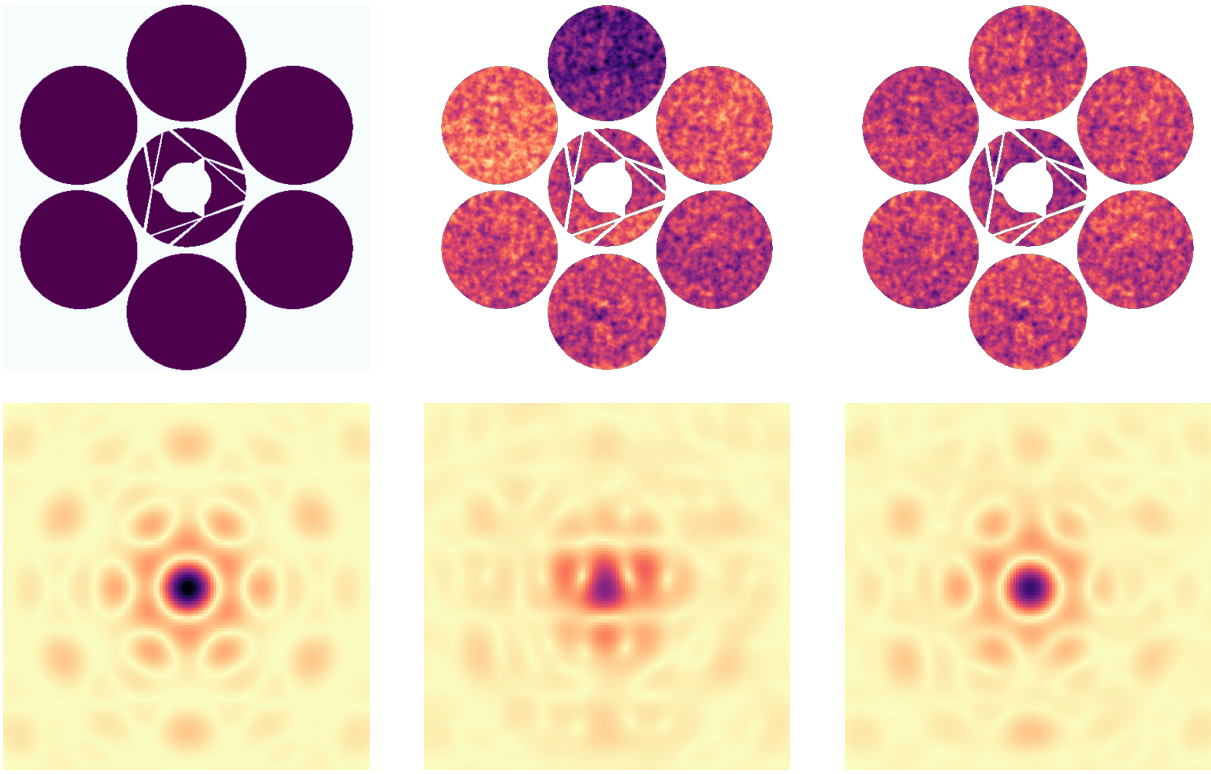

Figure 2: Wavefront errors (top) and corresponding PSF (bottom). Flat incoming wavefront (left), typical LTAO residual wavefront without (center) and with (right) segment piston control.

(i) Telescope phasing sensor,

(ii) M1 and M2 edge sensors, and

(iii) Segment piston sensor from tip-tilt images.

When acquiring a new target, there is an error in the rigid body motion of each segment.A facility telescope phasing sensor measures the segment piston errors caused by rigid-body motion errors of M1 and M2 and adjusts M1 segment piston and segment tip-tilt to compensate. These measurements are made using the Acquisition, Guiding and Wavefront Sensor (AGWS) system, consisting of four units operating between $6'$ and $10'$ from the optical axis. The phasing sensor uses a dispersed fringe sensor (DFS) at J-band at a frame rate of 0.033 Hz. The principle and performance of the DFS are described in detail in van Dam *et al.*[9,10] We expect a telescope segment piston error of approximately 100 nm RMS after convergence.

Once the telescope is coarsely phased, the M1 and M2 edge sensors are used to keep the telescope mirrors "stiff". However, changes in the temperature gradient in the M1 segments lead to slow changes in the positions of the edge sensors. Consequently, the telescope phasing sensor is required to continually monitor the phasing error by making measurements once every 30 s.

A description of the metrology system, including the M1 edge sensors, is found in Sitarski *et al.*[11] There are 48 relative distance measuring interferometer baselines mounted in pairs at 24 locations across the M1 segment gaps, as shown in Figure 3. These 48 measurements are used to reconstruct 42 rigid body motion terms, six for each segment. The M2 edge sensors are internal to the ASM and are not included in the simulations.

As previously mentioned, the LTWS is blind to segment piston errors. The wavefront reconstructor applies the segment piston commands that enforce the smoothest wavefront over the entire telescope consistent with the

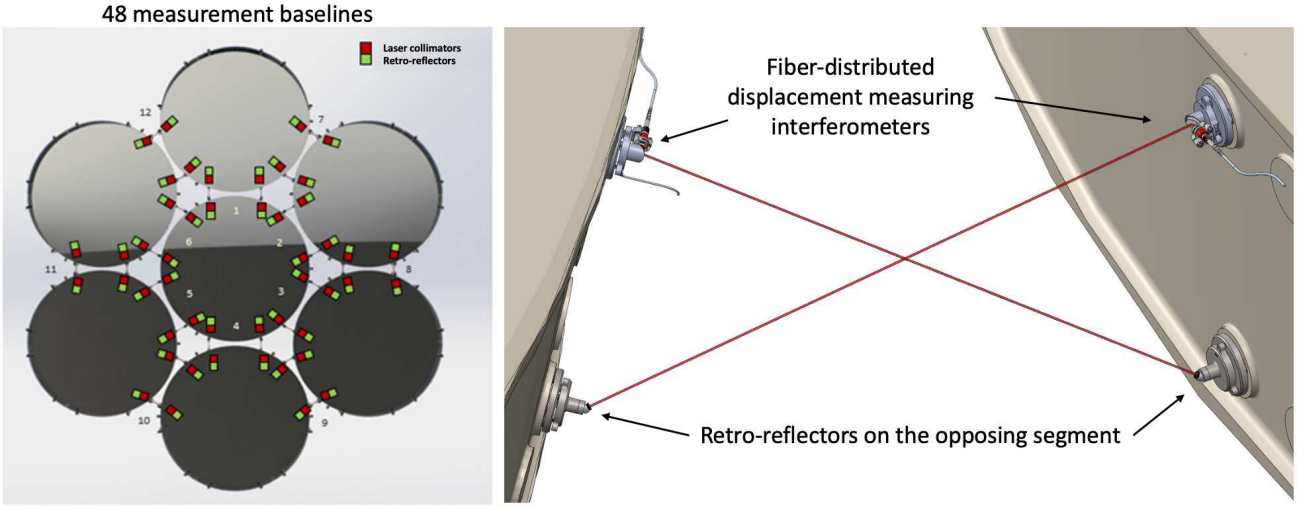

Figure 3: Schematic of the M1 edge sensors.

measured wavefront slopes. The atmospheric segment piston term arises from the fact that the true segment piston differs from this segment piston estimate and has a value of the order of 100 nm to 150 nm for typical atmospheric conditions and changes rapidly. Measurements of the order of 100 Hz or faster are needed to compensate for atmospheric segment piston. This paper explores the ability to make these measurements using tip-tilt sensor images.

3. PHASE RETRIEVAL ALGORITHMS

Phase retrieval is the term given to the process of deducing the phase of the complex amplitude of the electric field at the pupil plane based on a measurement at or near the focal plane. In this paper, we compare the performance of two algorithms: a modified implementation of the well-known Gerchberg-Saxton (G-S) algorithm,[5,6] and the Fast & Furious algorithm (henceforth referred to as F&F),[12,13] which has already found application in high-contrast astronomical AO systems. The implementation of both algorithms has been made freely available as a Python package named *pripy*.[14]

The mathematical principles underlying both phase retrieval techniques assumes monochromatic imaging of a point source. Nevertheless, both the F&F and G-S algorithms perform almost as well in simulations when using broadband images, and all the simulations in this report were made using broadband light. The implementations of the F&F and G-S algorithms are explained in Sect. 3.3 and Sect. 3.2 respectively, while Sect. 3.4 lists other potential algorithms that were not explored in this paper.

3.1 Preprocessing steps

Some preprocessing of the images is required before unleashing the G-S or F&F algorithms. The steps are:

(i) Extract a region of the image centered around the location of the tip-tilt star.

(ii) Recenter the image using FFT interpolation so it is centered as well as possible.

(iii) Threshold the pixel values to zero.

Recentering the image removes the mean tip-tilt in the phase, a term which we do not want to measure and reduces the dynamic range of the algorithms.

3.2 Sequential Gerchberg-Saxton algorithm

The Gerchberg-Saxton algorithm has a history spanning half a century since the seminal paper by Gerchberg and Saxton.[5] It consists of a very simple non-linear iterative algorithm that solves for the phase at the pupil plane based on knowledge about the amplitude at the pupil plane, $A_0(x, y)$, and a measurement of the amplitude at the image plane, $a_0(u, v)$, which is the square root of the measured image. The initial guess for the phase in the pupil plane, $\phi(x, y)$ usually consists of random pixel values uniformly distributed between $-\pi$ and π radians. For successive images, we have the option to begin with the phase estimate corresponding to the previous image (*i.e.*, a "warm start"), but this did not appear to reduce the convergence time. The complex amplitude at the pupil plane, $A_0(x, y) \exp[i\phi(x, y)]$, is used to compute the corresponding complex amplitude at the image plane, $a \exp[i\psi(u, v)]$. In what follows we drop the coordinates (x, y) and (u, v) for clarity. We write

$$a \exp[i\psi] = \mathcal{F}[A_0 \exp[i\phi]]. \tag{1}$$

where ψ represents the phase at the image plane and $\mathcal{F}$ represents the Fourier transform, computed using the Fast Fourier Transform (FFT) algorithm. The measured amplitude at the focal plane, a_0, replaces the calculated value, a, and the complex amplitude at the pupil plane is recomputed:

$$A \exp[i\phi] = \mathcal{F}^{-1}[a_0 \exp[i\psi]], \tag{2}$$

where $\mathcal{F}^{-1}$ denotes the inverse Fourier transform. The measured pupil amplitude, A_0, replaces the calculated amplitude, A, and the procedure iterates between Eq. (1) and Eq. (2), as depicted by Figure 4.

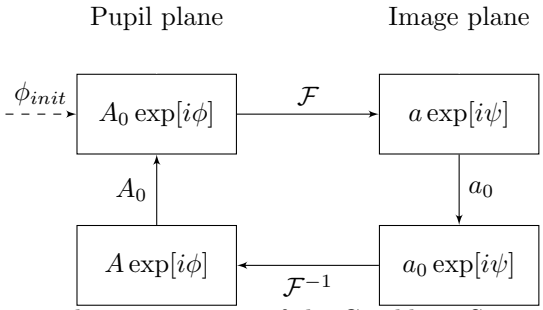

Figure 4: Pictorial representation of the Gerchberg-Saxton algorithm.

The Gerchberg-Saxton algorithm has the desirable property that it cannot diverge, and has been shown to be a steepest-descent algorithm.[6] Unfortunately, it can stagnate (*i.e.*, converge to a local minimum) or converge to a phase-wrapped solution.

In order to speed up the convergence and to reduce the possibility of converging to a local minimum, two modifications are made for the first 10 iterations of the algorithm. First, the amplitude of the image outside of the valid region where the signal-to-noise (SNR) ratio is high is forced to be zero: *i.e.*,

$$a_0(u, v) = \begin{cases} a_0(u, v), & \text{if } |u| \leq d \text{ and } |v| \leq d \\ 0, & \text{otherwise} \end{cases} \tag{3}$$

where d is the region of valid support. Driving the amplitude to zero outside the central region of the image improves the speed of convergence but introduces artefacts in the reconstructed phase. Second, the modifications known as the hybrid input-output algorithm are made. The equations Eq. (1) and Eq. (2) are replaced by:

$$a \exp[i\psi] = \mathcal{F}[(A_0 + h(A_0 - A)) \exp[i\phi]], \tag{4}$$

and

$$A \exp[i\phi] = \mathcal{F}^{-1}[(a_0 + h(a_0 - a)) \exp[i\psi]]. \tag{5}$$

where h is a constant with a typical value of 0.3. After 10 iterations, the value of h is set to 0 and the algorithm resumes for 10 more interations. However, the image pixels outside the valid support are no longer forced to zero, but are allowed to "float": *i.e.*,

$$a_0(u,v) = \begin{cases} a_0(u,v), & \text{if } |u| \le d \text{ and } |v| \le d \\ a(u,v), & \text{otherwise} \end{cases} \tag{6}$$

This step greatly reduces the level of artefacts in the reconstructed phase. This approach is similar to what is proposed in Fienup (1993), where a weighting is applied to the pixels in the image plane.[15]

The computation time for 20 iterations with calls to the CuPy library on an NVIDIA RTX A5000 GPU is 8.0 ms. We are confident that we can reduce the computation time to an acceptable value for real-time operation (approximately 0.5 ms) by running fewer iterations, coding directly in CUDA and upgrading the GPU.

The solution obtained by any phase retrieval based on a single image is not unique, as there are three changes that can be made to the phase that do not affect the amplitude at the focal plane:[16]

- Addition of a constant to $\phi(x,y)$.
- Addition of a multiple of 2π to any point in $\phi(\mathbf{x})$ for monochromatic light.
- Replacing $\phi(x,y)$ by $-\phi(-x,-y)$ if $A(x,y)$ is symmetrical.

The first point refers to the well-known fact that global piston does not affect the image. The second point leads to the possibility of phase wrapping, where there are discontinuous jumps of 2π radians in the solution. This can be detected and sometimes resolved using a process named phase unwrapping. The detection of phase wrapping in the solution was not implemented, while it is not clear whether phase unwrapping can be accomplished in real time. Finally, the so-called phase ambiguity problem arises for symmetrical pupils, where there are two solutions that are consistent with the measured intensity. To resolve the phase ambiguity, we need to use successive frames.

Let us define the two solutions at time k to be $\phi_1[k]$ and $\phi_2[k]$, and the corresponding least-squares projection of the phase onto a seven-element segment piston vector as $s_1[k]$ and $s_2[k]$. Assume that at time k, a change in the segment piston command is applied, which we denote as $\Delta c[k]$. At time $k+1$, we make a new measurement and obtain two new segment piston estimates, $s_1[k+1]$ and $s_2[k+1]$. We want to know which of these two estimates to use in updating the segment piston commands. The following four quantities are computed:

$$\begin{aligned} q_{11} &= \Sigma(s_1[k+1] - s_1[k] - \Delta c[k])^2 \\ q_{12} &= \Sigma(s_1[k+1] - s_2[k] - \Delta c[k])^2 \\ q_{21} &= \Sigma(s_2[k+1] - s_1[k] - \Delta c[k])^2 \\ q_{22} &= \Sigma(s_2[k+1] - s_2[k] - \Delta c[k])^2 \end{aligned} \tag{7}$$

where the summation is over the seven elements. If the quantity with the smallest value is q_{11} or q_{12}, we declare that $s_1[k+1]$ is the correct solution. Conversely, if the smallest value corresponds to q_{21} or q_{22}, then $s_2[k+1]$ is used as the segment piston estimate. We refer to this procedure as the *sequential Gerchberg-Saxton algorithm*.

3.3 Fast & Furious

The Fast & Furious algorithm was designed to measure quasi-static aberrations from high-contrast images corrected with adaptive optics,[12,17] and has enjoyed success on the telescope.[13] In contrast to the G-S algorithm, F&F produces a deterministic solution instead of an iterative one. F&F makes approximations in the imaging model, which lead to a low computational load but require phase deviations to remain within 1 rad peak-to-valley. In practice, even if the aberrations exceed this level, F&F converges in closed loop.[12]

The reader is referred to the paper by from Bos *et al.* which explains in detail the theory behind the algorithm and the implementation.[13] Here, we do not explain the origin of the equations, but describe the procedure using the same notation. Figure 5 represents the Fast & Furious algorithm pictorially.

The measured image, $p(u,v)$, is split into the odd and even components, $p_o(u,v)$ and $p_e(u,v)$ respectively:

$$p(u,v) = p_o(u,v) + p_e(u,v), \tag{8}$$

where

$$p_o = (p(u,v) - p(-u,-v))/2, \tag{9}$$

and

$$p_e = (p(u,v) + p(-u,-v))/2. \tag{10}$$

For compactness of notation, we proceed to drop the (u,v) argument.

The amplitude at the pupil plane is A, $a = \mathcal{F}[A]$, and a^2 is the diffraction-limited PSF. The estimated Strehl of the image is S. We solve

$$y = \frac{ap_o}{2a^2 + \epsilon}, \tag{11}$$

and

$$|v| = \sqrt{|p_e - (Sa^2 + y^2)|}. \tag{12}$$

There are two parameters in the code that can be adjusted: the regularization parameter, ϵ, which depends on the noise level of each pixel, and the value of the estimated Strehl. It was found that the value of S that produces the best reconstruction is slightly higher than the actual Strehl of the image.

This solves for the absolute value of v, but the sign is unknown due to phase ambiguity. To find the sign, we use the even component of previous image, $p_{i-1,e}$ and the quantities

$$y_d = i\mathcal{F}[A\phi_{d,o}] \tag{13}$$

and

$$v_d = \mathcal{F}[A\phi_{d,e}] \tag{14}$$

where ϕ_d is the diversity between the images (*i.e.*, the change in segment piston commands) and the subscripts refer to its even and odd components. The constant i is the square root of -1.

We compute the sign of v as

$$\text{sign}(v) = \frac{p_{i-1,e} - p_{i,e} - (v_d^2 + y_d^2 + 2yy_d)}{2v_d}. \tag{15}$$

At the first iteration, before any diversity is applied, we set $\text{sign}(v) = a$.

The pupil-plane phase estimatem ϕ, is given by:

$$A\phi = \mathcal{F}^{-1}[\text{sign}(v)|v| - iy]. \tag{16}$$

The conversion from an image to a phase estimate takes 4.3 ms, which is twice as fast as the G-S algorithm.

3.4 Other fast phase retrieval implementations

In this section, we list alternative phase retrieval implementation.

Cranney *et al.* proposed a novel method for retrieving the segment piston, based on the Moving Horizon Estimation (MHE) algorithm.[4] Briefly, MHE is generally a non-linear optimisation problem that uses statistics of the temporal evolution of the segment piston error to regularize the solution. In this paper, we shelve the use of the MHE because of the results obtained using MHE to date do not warrant the large increase in computational complexity.[4]

For completeness, we also describe other linear solutions to the phase retrieval problem that have been reported in the literature and tested experimentally. The LInearised Focal-plane Technique (LIFT)[18] applies a known static aberration to the wavefront, which, for sufficiently small wavefront perturbations, both resolves the

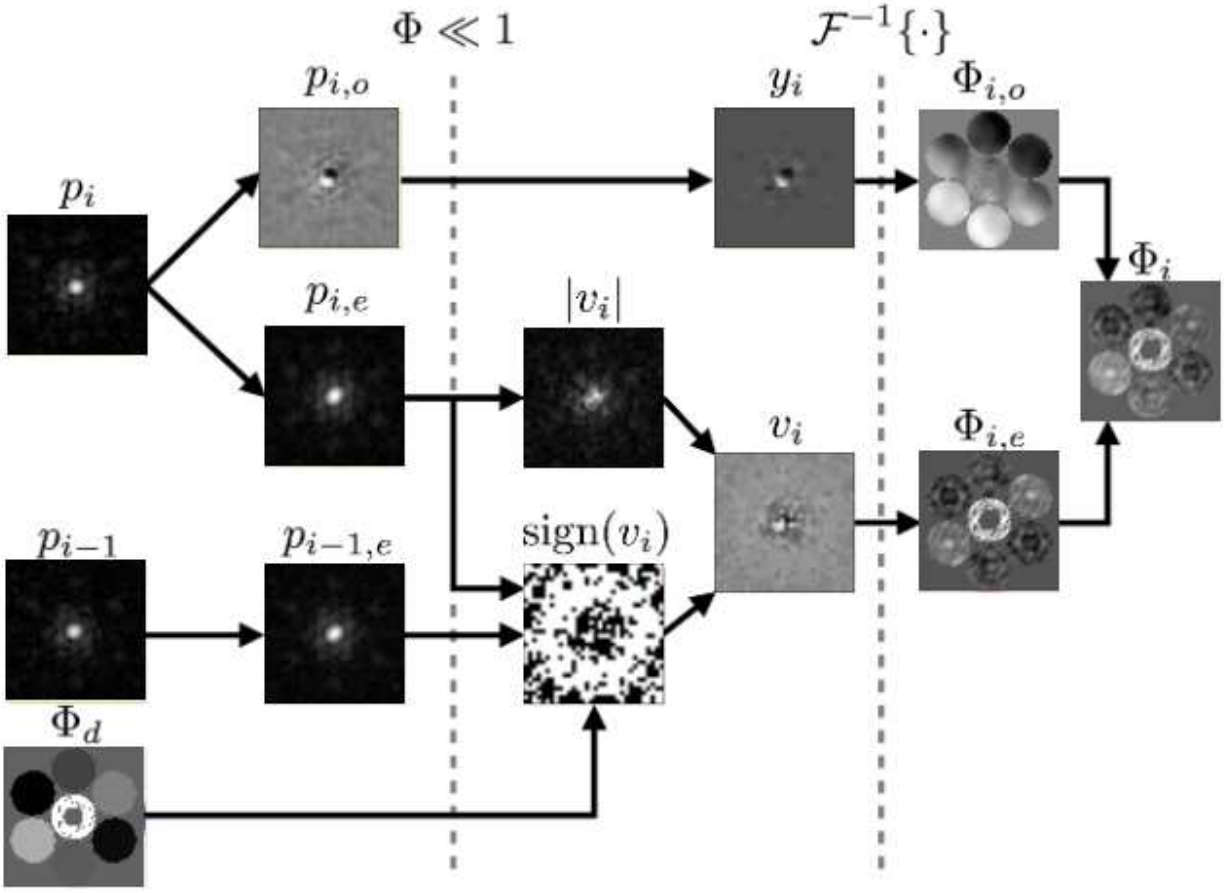

Figure 5: Schematic representation of the Fast & Furious algorithm, adapted from Bos *et al.*[13]

phase ambiguity and converts the measured intensity into a linear function of wavefront modes. Plantet *et al.* demonstrate the use of LIFT for estimating segment piston of the GMT in simulations.[19]

A similar game can be played by applying a mask to the pupil to break its symmetry. For an asymmetric pupil and small phase errors (1 rad or less), a linear relationship can be derived between the wavefront and the intensity.[20] This relationship is widely used in intereferometry, where it is known as kernel phase.

LIFT and kernel phase have the advantage that they compute the phase very rapidly. However, the disadvantage of both these methods is that they require a modification to either the phase or the amplitude at the pupil, and that the solution is a linear approximation that is only valid for small phase errors. The GS algorithm, by contrast, works for any phase errors (at least in the monochromatic case).

4. SIMULATION DESCRIPTION

The performance of the phase retrieval algorithms was evaluated using end-to-end simulations in the CEO environment,[21] a simulation tool written specifically to model the optical behavior of the GMT. The simulations were written in Python and use GPU processing for speed. In this section, we describe the simulations in detail.

4.1 Disturbances

There are three sets of disturbances in these simulations: atmospheric turbulence, telescope wind shake and a static telescope phasing error.

The atmospheric parameters are derived from the typical-typical profile for January 2008 from Goodwin[22] and are reproduced in Table 1. This turbulence profile has a higher fraction of turbulence in the free atmosphere

Table 1: Turbulence profile used in the simulations.

Elevation (m)	Turbulence fraction	Wind speed (m/s)	Wind direction (°)
25	0.126	5.65	0.78
275	0.087	5.80	8.25
425	0.067	5.89	12.48
1250	0.350	6.64	32.50
4000	0.227	13.29	72.10
8000	0.068	34.83	93.20
13000	0.075	29.42	100.05

compared to profiles from other studies, including those measured by the same author four months earlier. This leads to strong angular anisoplanatism, which is compensated in the tip-tilt sensor using a dedicated DM. Unless otherwise specified, the value of r_0 is 0.16 m at a wavelength of 500 nm at zenith with an outer scale of 25 m, median values for the site. All of the simulations were run at a zenith angle of 30°.

The telescope windshake model was derived using finite element modeling of the telescope and its environment. The output consists of time series of the M1 and M2 rigid body motions (three translations and three rotation modes for each segment) as well as the deformation of the M1 primary mirror segments. The windshake data used in this paper corresponds to a typical observation at a zenith angle of 30°, with a $7\,\mathrm{m\,s^{-1}}$ wind at an azimuth of 45°, median for the site.

In addition to the disturbances caused by turbulence and wind shake, there is a random static segment piston wavefront error with a magnitude of 100 nm RMS.

4.2 Wavefront sensors

Two wavefront sensing units are simulated: the laser tomography WFS (LTWS) and the tip-tilt sensor.

The LTWS consists of six Shack-Hartmann WFS with 60×60 lenslets across the pupil. The LGSs are projected in a regular hexagonal constellation on the sky at an off-axis distance of 30″. Physical optics are used to model the WFSs, but there is no LGS elongation in the model, so the noise on the slope estimates is negligible.

The detector for the tip-tilt sensor is assumed to be the SAPHIRA, an infrared e-APD array produced by Leonardo.[23,24] The photometry and noise parameters used for the tip-tilt sensor are tabulated in Table 2. The throughput to the tip-tilt sensor depends on whether GMTIFS (60%) or GMTNIRS (6%) is used.

Table 2: Photometric parameters used in the simulations.

Parameter	Value
Central wavelength	2.179 µm
Bandwidth	0.41 µm
Photometric zero point	7.0×10^{11}
Sky background (magnitude / arcsec^2)	12.71
Optical throughput	60% or 6%
Quantum efficiency	72%
Excess noise factor	1.35
Read noise	$0.4e^-$
Dark current	$10e^-$

An open-loop M1 edge sensor is used to sense the rigid-body motions of the M1 segments, and the disturbances are compensated using M2 ASM commands.

4.3 Wavefront control

The simulations were run for a total of 5 s at a rate of 500 Hz. The feedback control loops were modeled as an integral controller with a loop gain of 0.6. There was also a pure delay of one cycle, which was added to the one cycle inherent in the camera stare and the zero-order hold of the wavefront corrector.

The high-order reconstructor consists of a minimum-variance tomographic reconstructor operating in pseudo open-loop. The tip-tilt loop and segment piston are controlled using a least-squares reconstructor in closed-loop.

Two wavefront correctors are used in the simulations. The adaptive secondary mirror (ASM) is in the common path and corrects the wavefront incident on the science instrument as well as all of the WFSs. The first 200 Karhunen-Loéve modes are corrected for each of the seven segments, for a total of 1400 modes.

For GMTIFS, where the NGS is between 15″ and 90″ off-axis, there is an additional dedicated deformable mirror (DM) on the path of the tip-tilt sensor only. This DM sharpens the spot on the tip-tilt sensor and makes segment piston estimation possible. The DM is modeled as a 32×32 actuator device, with a smooth influence function between actuators.

The temporal dynamics of both the ASM and the DM were deemed negligible for this study.

5. SIMULATION RESULTS

In this section, we present the simulation results using an on-axis and an off-axis tip-tilt sensor in Sections 5.1 and 5.2 respectively.

5.1 On-axis simulations

In this section, we run on-axis simulations corresponding to GMTNIRS, which uses an on-axis tip-tilt sensor guiding on 10% of the K-band light. An example of the phase retrieval process is shown in Figure 6. The residual wavefront is shown three time steps after the segment piston loop is closed, with some residual segment piston. Figure 6 displays the residual wavefront, the tip-tilt sensor image, and the reconstructed wavefronts using the G-S and F&F algorithms.

The highest measurable spatial frequencies are dictated by the number of image pixels used in the phase retrieval. In this case, a region of 20×20 pixels is extracted from the images, which is a typical value. Increasing the number of used pixels leads to a noisier but higher resolution reconstruction, but recall that we are only interested in estimating the segment piston values and not the true wavefront error. The performance as a

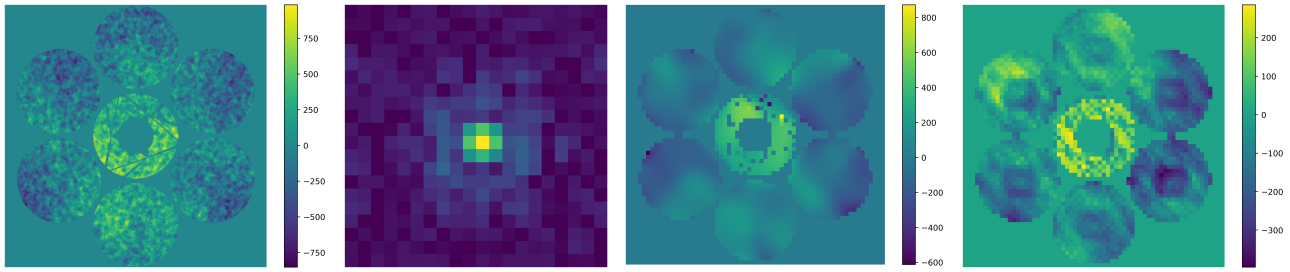

Figure 6: From left to right: residual wavefront, tip-tilt sensing image, wavefront reconstructed using G-S and F&F algorithms. All of the wavefront errors are reported in nm.

function of r_0 was simulated to determine whether the segment piston can be measured over a wide range of conditions. Simulations were run without any segment piston estimation, with a perfect segment piston measurement made directly by inspection of the residual wavefront, and using the G-S and F&F algorithms. The simulation results, tabulated in Table 3 and plotted in Figure 7, show that both of the phase retrieval algorithms produce almost ideal performance when guiding on a bright on-axis guide star over a wide range of atmospheric conditions.

Table 3: RMS wavefront error (nm) for different segment piston sensing strategies for a bright on-axis tip-tilt star.

r_0 (m)	0.08	0.10	0.12	0.16	0.20
Ideal segment piston sensor	300	250	216	172	144
Sequential Gerchberg-Saxton	307	256	222	179	151
Fast & Furious	309	257	222	177	149
No segment piston sensor	387	321	277	223	191

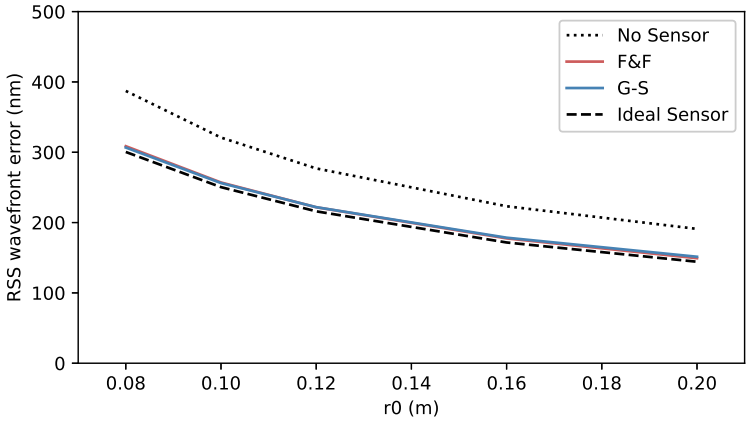

Figure 7: RMS wavefront error as a function of r_0 for an observation at a zenith angle of 30° guiding on a on-axis bright star. The simulations were run without any segment piston sensing as well as sensing segment piston with the G-S algorithm, the F&F algorithm and an ideal segment piston sensor.

The performance over a range of guide star magnitudes was evaluated (Figure 8). The tip-tilt sensor operates at 500 Hz for all guide star magnitudes for ease of comparison. For on-sky operation, we would reduce the frame rate and/or coadd frames to increase the SNR before computing the segment piston error. Because the tip-tilt measurement is also impacted by measurement noise, the correction degrades even for the cases where there is no segment piston measurement or the segment piston measurement is ideal. The limiting magnitude of the F&F

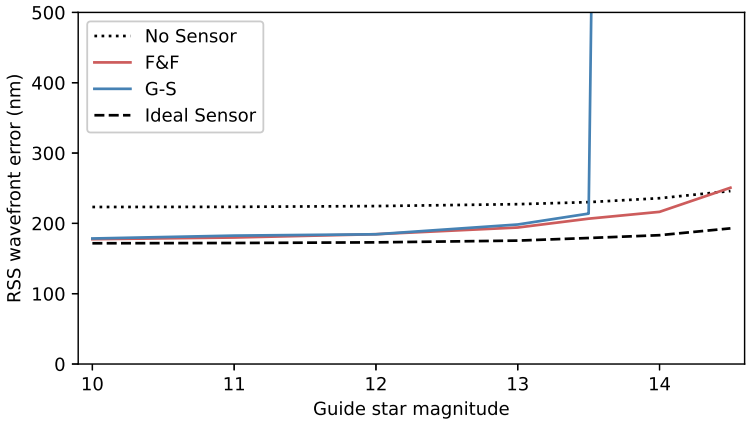

Figure 8: RMS wavefront error as a function of guide star magnitude for an r_0 of 0.16 m for an observation at a zenith angle of 30° using an on-axis guide star. The simulations were run without any segment piston sensing as well as sensing segment piston with the G-S algorithm, the F&F algorithm and an ideal segment piston sensor. All measurements were made at 500 Hz.

algorithm is higher than that of the G-S. Crucially, it also appears to fail more gracefully beyond its limiting magnitude.

The dynamic range was evaluated. Both algorithms were able to recover segment pokes of up to $\lambda/2$ under favourable conditions (bright guide star, r_0 of 0.16 m). Segment pokes larger than this lead to phase wrapping, where the poked segment is driven to a segment piston of one wave, and the use of the telescope phasing sensor (AGWS) is required to restore the displaced segment.

It was feared that unknown variations in the amplitude at the pupil plane could lead to errors in the reconstruction. In particular, some segments could have coatings applied more recently than others, leading to variations in the reflectivity. A numerical experiment was run where the reflectivity of each segment was varied by 10% RMS, with the variation not known by the phase retrieval algorithms. This change in amplitude did not affect the performance of either the G-S or the F&F algorithms.

5.2 Off-axis simulations

Here, we report on the simulations results for GMTIFS, where the OIWFS picks off all of the light from a star located between 15″ and 90″ from the optical axis and directs the K-band light to the tip-tilt sensor.

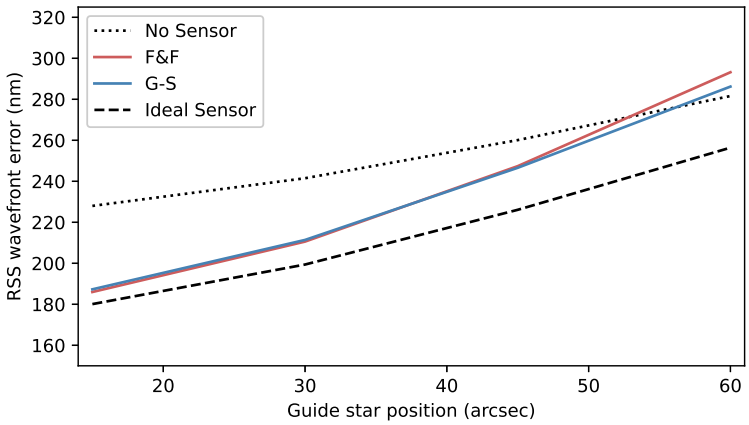

Figure 9: RMS wavefront error as a function of off-axis distance for an observation using a bright guide star at a zenith angle of 30° with r_0 =0.16 m. The simulations were run without any segment piston sensing as well as sensing segment piston with the G-S algorithm, the F&F algorithm and an ideal segment piston sensor.

The performance as a function of off-axis distance is plotted in Figure 9. The segment piston sensor is useful over the range 15″-45″ in median seeing conditions. For guide stars further away, two factors conspire to reduce the effectiveness of the segment piston sensor. First is the unavoidable fact that atmospheric segment piston has a strong angular dependence. As the distance from the optical axis increases, even perfect off-axis measurements provide an increasingly unreliable representation of the on-axis segment piston error. Secondly, the degradation in image quality due to high-order anisoplanatism leads to increasing errors in the segment piston estimate. Both of these factors depend on the strength and vertical distribution of the turbulence.

Next, we consider the performance with varying values of r_0 for a guide star 30″ off-axis (Figure 10). The G-S algorithm is more tolerant to wavefront errors than the F&F and can operate in the presence of larger residual wavefront errors.

Finally, we consider how the algorithms perform with varying guide star magnitudes when the value of r_0 is fixed to 0.16 m. Once again, the simulations show that the F&F algorithm has a higher limiting magnitude ($m_K \leq 16.5$) than the G-S algorithm ($m_K \leq 15$) when estimating segment piston at 500 Hz. Both algorithms can run slower using fainter stars, but this is not quantified in this paper.

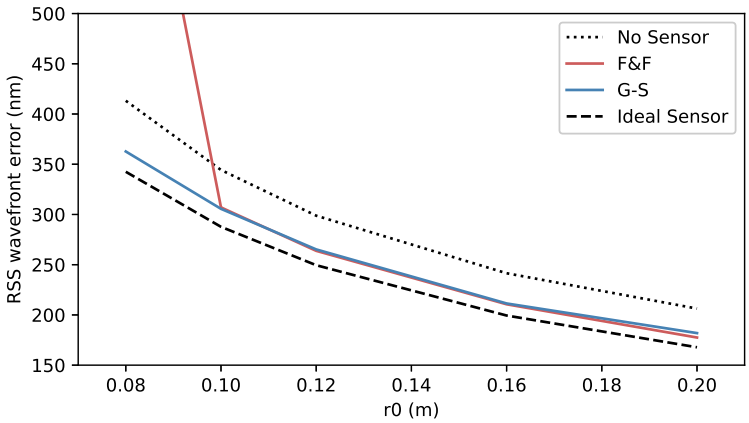

Figure 10: RMS wavefront error as a function of r_0 for a bright guide star 30″ off-axis at a zenith angle of 30°. The simulations were run without any segment piston sensing as well as sensing segment piston with the G-S algorithm, the F&F algorithm and an ideal segment piston sensor.

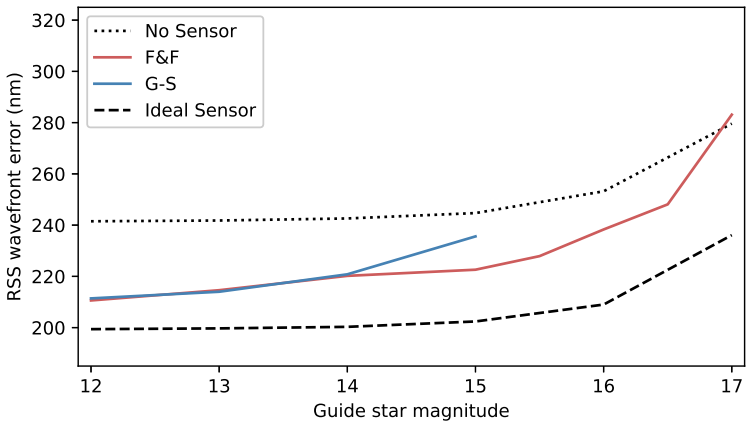

Figure 11: RMS wavefront error as a function of guide star magnitude for a guide star 30″ off-axis at a zenith angle of 30°. The simulations were run without any segment piston sensing as well as sensing segment piston with the G-S algorithm, the F&F algorithm and an ideal segment piston sensor.

6. CONCLUSION

The laser tomography wavefront sensor planned for the GMT's LTAO system is blind to segment piston errors. In this paper, we propose a way to measure segment piston errors using images from the tip-tilt sensor, a Nyquist sampled eAPD imager operating in the K-band. Two algorithms are compared: the sequential Gerchberg-Saxton algorithm and the Fast & Furious algorithm. In most respects, the performance of the algorithms is similar, and either one could be used over a large range of observing conditions. The F&F algorithm appears to be more robust to measurement noise and able to operate with fainter guide stars up to one magnitude fainter. The G-S algorithm, on the other hand, is more robust to residual wavefront errors and can thus operate in worse seeing and further off-axis.

Further algorithmic development is required to run phase retrieval under challenging conditions (high residual wavefronts and low SNR). In particular, a supervisory process is required to determine whether the segment piston estimate produced by the algorithms is likely to be useful, or whether the measurement should be rejected. Nevertheless, phase retrieval appears to be a very promising solution to a challenging wavefront sensing problem for the GMT.

REFERENCES

[1] A. H. Bouchez, D. S. Acton, R. Biasi, *et al.*, "The Giant Magellan Telescope adaptive optics program," in *Adaptive Optics Systems IV*, **9148**, 300–318, SPIE (2014).

[2] R. Sharp, D. Adams, G. Bloxham, *et al.*, "Design evolution of the Giant Magellan Telescope integral field spectrograph, GMTIFS," in *Ground-based and Airborne Instrumentation for Astronomy VII*, **10702**, 597–608, SPIE (2018).

[3] D. T. Jaffe, S. Barnes, C. Brooks, *et al.*, "GMTNIRS: progress toward the Giant Magellan Telescope near-infrared spectrograph," in *Ground-based and Airborne Instrumentation for Astronomy VI*, **9908**, 648–656, SPIE (2016).

[4] J. Cranney, F. Rigaut, R. Sharp, *et al.*, "Segment phasing for giant telescopes using moving horizon estimation," in *Adaptive Optics Systems VIII*, **12185**, 1633–1642, SPIE (2022).

[5] R. W. Gerchberg and W. O. Saxton, "A practical algorithm for the determination of plane from image and diffraction plane pictures," *Optik* **35**(2), 237–246 (1972).

[6] J. R. Fienup, "Phase retrieval algorithms: a comparison," *Appl. Opt.* **21**, 2758–2769 (1982).

[7] A. H. Bouchez, R. Conan, R. T. Demers, *et al.*, "Overview and status of the GMT wavefront control system," in *Adaptive Optics Systems VIII*, **12185**, 401–421, SPIE (2022).

[8] F. Quirós-Pacheco, M. van Dam, A. H. Bouchez, *et al.*, "The Giant Magellan Telescope natural guidestar adaptive optics mode: improving the robustness of segment piston control," in *Adaptive Optics Systems VIII*, **12185**, 348–360, SPIE (2022).

[9] M. A. van Dam, B. A. McLeod, and A. H. Bouchez, "Dispersed fringe sensor for the Giant Magellan Telescope," *Applied Optics* **55**(3), 539–547 (2016).

[10] D. Kopon, B. McLeod, A. Bouchez, *et al.*, "Preliminary on-sky results of the next generation gmt phasing sensor prototype," in *Adaptive Optics Systems VI*, **10703**, 300–313, SPIE (2018).

[11] B. N. Sitarski, A. Rakich, H. Chiquito, *et al.*, "The GMT telescope metrology system design," in *Ground-based and Airborne Telescopes IX*, **12182**, 54–70, SPIE (2022).

[12] V. Korkiakoski, C. U. Keller, N. Doelman, *et al.*, "Fast & furious focal-plane wavefront sensing," *Appl. Opt.* **53**(20), 4565–4579 (2014).

[13] Bos, S. P., Vievard, S., Wilby, M. J., *et al.*, "On-sky verification of Fast and Furious focal-plane wavefront sensing: moving forward toward controlling the island effect at Subaru/SCExAO," *A&A* **639**, A52 (2020).

[14] J. Cranney, "Phase Retrieval In PYthon." https://github.com/jcranney/pripy (2022).

[15] J. R. Fienup, "Phase-retrieval algorithms for a complicated optical system," *Applied optics* **32**(10), 1737–1746 (1993).

[16] R. Lane, W. Fright, and R. Bates, "Direct phase retrieval," *IEEE transactions on acoustics, speech, and signal processing* **35**(4), 520–526 (1987).

[17] C. U. Keller, V. Korkiakoski, N. Doelman, *et al.*, "Extremely fast focal-plane wavefront sensing for extreme adaptive optics," in *Adaptive Optics Systems III*, **8447**, 749–758, SPIE (2012).

[18] S. Meimon, T. Fusco, and L. Mugnier, "LIFT: A focal-plane wavefront sensor for real-time low-order sensing on faint sources," *Optics Letters* **35**(18), 3036–3038 (2010).

[19] A.-L. Cheffot, C. Plantet, E. Pinna, *et al.*, "Differential piston sensing with LIFT: application to the GMT," in *Astronomical Telescopes and Instrumentation*, International Society for Optics and Photonics, SPIE (2022).

[20] F. Martinache, "The asymmetric pupil Fourier wavefront sensor," *Publications of the Astronomical Society of the Pacific* **125**(926), 422 (2013).

[21] R. Conan, "Cuda Engined Optics." https://github.com/rconan/CEO (2022).

[22] M. S. Goodwin *et al.*, "Turbulence profiling at siding spring and las campanas observatories," (2009).

[23] D. Atkinson, D. Hall, C. Baranec, *et al.*, "Observatory deployment and characterization of saphira hgcdte apd arrays," in *High Energy, Optical, and Infrared Detectors for Astronomy VI*, **9154**, 405–416, SPIE (2014).

[24] G. Finger, I. Baker, D. Alvarez, *et al.*, "Saphira detector for infrared wavefront sensing," in *Adaptive Optics Systems IV*, **9148**, 427–442, SPIE (2014).